

Modeling of Adsorption and Nucleation in Infinite Cylindrical Pores by Two-Dimensional Density Functional Theory

E. A. Ustinov[†] and D. D. Do^{*}

Department of Chemical Engineering, University of Queensland, St. Lucia, Queensland, Brisbane, 4072 Australia

Received: February 16, 2005; In Final Form: April 17, 2005

In this paper, we present an analysis of argon adsorption in cylindrical pores having amorphous silica structure by means of a nonlocal density functional theory (NLDFT). In the modeling, we account for the radial and longitudinal density distributions, which allow us to consider the interface between the liquidlike and vaporlike fluids separated by a hemispherical meniscus in the canonical ensemble. The Helmholtz free energy of the meniscus was determined as a function of pore diameter. The canonical NLDFT simulations show the details of density rearrangement at the vaporlike and liquidlike spinodal points. The limits of stability of the smallest bridge and the smallest bubble were also determined with the canonical NLDFT. The energy of nucleation as a function of the bulk pressure and the pore diameter was determined with the grand canonical NLDFT using an additional external potential field. It was shown that the experimentally observed reversibility of argon adsorption isotherms at its boiling point up to the pore diameter of 4 nm is possible if the potential barrier of $22kT$ is overcome due to density fluctuations.

1. Introduction

The classical representation of capillary condensation and evaporation in cylindrical pores is well established in the literature.^{1,2} According to this representation, the capillary condensation occurs at the gaslike spinodal pressure, where the system loses its mechanical stability. The capillary evaporation from the open ended cylindrical pore occurs at the equilibrium transition pressure via receding menisci from the pore ends toward each other. First attempts of quantitative description of the phenomena were based upon the Kelvin-like equations with the adsorbed film thickness accounted for.³ The modified Kelvin–Cohan equations have been widely used in the pore size distribution analysis (PSD), for example in the classical work of Barrett, Joyner, and Halenda (BJH).⁴ A more thermodynamically grounded mathematical model was developed by Broekhoff and de Boer (BdB).^{5,6} This theory uses adsorption data of nonporous reference material to determine adsorption in porous materials. It remains the most elegant and rigorous classical model. Since its inception in 1967, many attempts to improve this theory have been made in the literature. Lukens et al.⁷ simplified the BdB theory using the Hill approximation for the solid–fluid potential. Zhu et al.⁸ and Qiao et al.^{9,10} introduced an empirical curvature dependent potential, whereas Bhatia and co-workers^{11–15} accounted for the dependence of the surface tension on the meniscus curvature. It has allowed these authors to obtain the hysteresis critical diameter below which the isotherm is reversible, which is not possible in the original BdB theory. More fundamental analysis of the capillary phenomena was provided by molecular approaches, which are Monte Carlo (MC) technique^{16–19} and the nonlocal density functional theory (NLDFT).^{20–30} The discovery of high-ordered mesoporous MCM-41 materials^{31,32} gave an opportunity to

check the validity of different models. It was found that some features defy an easy explanation. For example, the reversibility of the nitrogen adsorption isotherm is experimentally observed up to the pore diameter of 4 nm,^{33–35} whereas the NLDFT gives a value 2 nm.²¹ Furthermore, there is also some controversy about which branch of the experimental isotherm is equilibrium. Morishige et al.^{36,37} came to the conclusion that the adsorption branch of the isotherm corresponds to the true thermodynamic equilibrium by analysis of the chemical potential dependence on temperature. This dependence is described with a straight line for the condensation pressure, whereas in the case of evaporation pressure, it exhibits a kink at the critical hysteresis temperature (see Figure 4 in ref 37). Some evidence supporting this viewpoint may be found in refs 38–40. The disappearance of the hysteresis below the hysteresis critical pressure is often attributed to the intrinsic pore size distribution, which induces nucleation at pressures below the vaporlike spinodal pressure^{41,42} or to the energetic heterogeneity of the pore wall surface.¹⁶ Another reason for the shift of the capillary condensation pressure toward lower values is the nucleation due to the density fluctuations.^{17–18,43–44} It should be mentioned that in the majority the consideration of the capillary phenomena by continuum approaches and with NLDFT is one-dimensional. However, the adequate representation of the formation of liquid bridges, bubbles, and the density rearrangement during condensation and evaporation may be achieved only in the framework of the two-dimensional version of the NLDFT to account for the variation of density in the radial and axial directions. The failure of the NLDFT to predict the critical pore size is usually attributed to its application to one-dimensional problems.¹³ This is a reason in the present paper the two-dimensional version of the NLDFT (i.e., accounted for the radial and axial density distributions) is applied to an infinite cylindrical pore. The 2D NLDFT is used to determine the mechanism of fluid distributions at the vaporlike and liquidlike spinodal pressures, as well as the disappearance of the smallest bridge

^{*} To whom correspondence should be addressed.

[†] On leave from Saint Petersburg State Technological Institute (Technical University), 26 Moskovsky Prospect, 198013, Russia.

and bubble at the limiting points of their mechanical stability. The second goal is to determine the Helmholtz free energy of the meniscus separating the liquidlike and gaslike fluids in the cylindrical pore. These two goals will be achieved using the canonical 2D NLDFT. The third goal is the calculating of the energy needed to nucleate condensation at different bulk pressures and pore diameters, which will be accomplished with the grand canonical 2D NLDFT (i.e., for the open pore that is allowed exchanging mass and energy with the surrounding).

2. Model

2.1. Density Functional Theory in the Case of Adsorption on Amorphous Solids. There are two reasons for the use of an advanced version of the NLDFT when applied to modeling of adsorption on amorphous solids. The first reason is that the two-dimensional NLDFT based on the conventional definitions of the solid–fluid potential and the excess Helmholtz free energy via the Carnahan–Starling equation for the equivalent hard sphere fluid leads to the solidification of the fluid in the cylindrical pore.⁴⁵ The solidification is caused by a strong molecular layering along the radial direction. It does not have any consequences in the framework of a one-dimensional task, but in the two-dimensional case the radial layering provokes the axial density redistribution followed by the appearance of the hexagonally packed dense concentric rings. Such an ordered solidlike configuration corresponds to a lower value of the Helmholtz free energy and probably could occur in the case of adsorption in carbon nanotubes due to the crystalline structure of the pore walls. However, in the case of adsorption in siliceous porous materials, the solidification of the adsorbed fluid at a temperature lower than the triple point is an artifact. The second reason is that the conventional NLDFT fits the experimental isotherms on nonporous silica and in cylindrical pores of MCM-41 samples very poorly. It is common to attribute the failure of the NLDFT to the energetic heterogeneity of the silica surface. However, our NLDFT analysis of nitrogen and argon adsorption isotherms on nonporous silica incorporating the energetic heterogeneity in the framework of patchwise model did not provide any good correlation.⁴⁶ This discrepancy indicates that a fundamental drawback is inherent in the way of the traditional application of the NLDFT to amorphous solids. From our viewpoint, the drawback is that the locus of solid–fluid potential minima is a perfect 2D surface (without any ripples) located at a distance of about one solid–fluid collision diameter from the solid surface. Such a perfect 2D surface is not physically expected for amorphous solids, as a rippled surface is a more likely candidate for these solids. The consequence of the perfect 2D surface is that fluid molecules “fall” into the potential minima surface forming a 2D molecular layer, which in turn, becomes a source of a secondary potential field having minimum at a distance of about one collision diameter from this layer. Consequently, a second layer is formed, and when pressure is increased more layers are formed, leading to steplike isotherms for low temperatures. This steplike isotherm was not observed, rather experimental isotherms are quite smooth. This discrepancy may be overcome if the fluid–fluid and solid–fluid interactions are considered in the same framework of the NLDFT. In this case, the solid is represented as a kind of frozen liquid of constant smoothed density. In our previous works^{46–49} we have successfully applied the original Tarazona’s version of the NLDFT to modeling of nitrogen and argon adsorption on nonporous silica and in MCM-41 cylindrical pores in the framework of one-dimensional model. In both cases, we achieved excellent correlation of adsorption isotherms over the

TABLE 1: Molecular Parameters for the System Ar–Silica at 87.3 K

fluid – fluid			solid – fluid	
σ_{ff} (nm)	d_{HS} (nm)	ϵ_{ff}/k_B (K)	σ_{sf} (nm)	$\rho_s \epsilon_{sf}/k_B$ (K nm ^{−3})
0.3305	0.3380	118.05	0.3127	6406

pressure range of 5–6 orders of magnitude. The key point of the approach is the interpretation of the excess Helmholtz free energy (which models repulsive forces between molecules) as a function of smoothed void volume instead of the smoothed density. Such interpretation is exactly equivalent to the Tarazona smoothed density approximation^{50–52} and uses the same weighting functions in the Tarazona’s prescription for weighted average.⁵² However, in the proximity of the pore wall, the smoothed void volume is decreased according to our new interpretation. Such a description allows us to model the contribution of solid atoms at a rough surface. The decrease of the smoothed void volume in the proximity of the solid (at a distance closer than approximately 2 collision diameters) allows accounting for the repulsive forces acting between the solid and the fluid. To model the excess Helmholtz free energy, we use the Carnahan–Starling (CS) equation⁵³ for the equivalent hard sphere fluid, which is applied in the original Tarazona’s theory.

Since in the developed approach the repulsive term for the solid–fluid interaction is already accounted for in the excess Helmholtz free energy, there is no need to account for this the second time in the solid–fluid LJ pair potential. Instead, we use the same Weeks–Chandler–Andersen (WCA) perturbation scheme⁵⁴ to account for only attractive term both for fluid–fluid and fluid–solid interactions. The solid–fluid molecular parameters (the collision diameter and the potential well depth) were determined by the least squares technique. We matched the calculated and experimental argon adsorption isotherms on nonporous silica⁵⁵ by minimizing the relative mean error. This matching allows us to properly describe the isotherm over the entire range of pressure. In the case of argon adsorption on silica surface at 87.3 K the molecular parameters used in the developed approach are listed in Table 1.

In Table 1, σ is the collision diameter, ϵ is the potential well depth, and ρ_s is the solid density. The subscripts ‘ff’ and ‘sf’ denote fluid–fluid and solid–fluid interaction, respectively. The fluid–fluid parameters were taken from.²² The cutoff distance is $5\sigma_{ff}$ for fluid–fluid interaction and $4.4\sigma_{sf}$ for fluid–solid interaction. Further details of the new approach of NLDFT to the solid–fluid interface may be found elsewhere.^{46–49}

2.2. Accounting for the Radial and Axial Density Distribution in the NLDFT. We used a cylindrical simulation cell having a length of 20 fluid–fluid collision diameters. The mirror-image conditions were applied at the two boundaries of the cell. The pore volume and pore walls were discretized by dividing the axis and the radius into equal segments having a thickness of one tenth of the collision diameter. Thus, the fluid and the solid were represented as a set of concentric rings. For each pair of rings, we defined the discrete set of Tarazona’s weight functions and that of WCA potentials as a 3-parametric function of their radii and the difference of their respective axial positions.

2.3. NLDFT in Canonical Ensemble. In the canonical ensemble, the amount adsorbed in the cylindrical simulation cell is specified. Let the number of molecules in the pore be n , which is the sum of $n_{j,k}$ ($j = 1:N$, $k = 1:M$). Here j and k are the numbers of the concentric rings counted along the radial and axial directions, respectively. Each value $n_{j,k}$ is proportional to the fluid density $\rho(r,z)$, with $r = j\delta r$ and $z = k\delta z$ (we choose

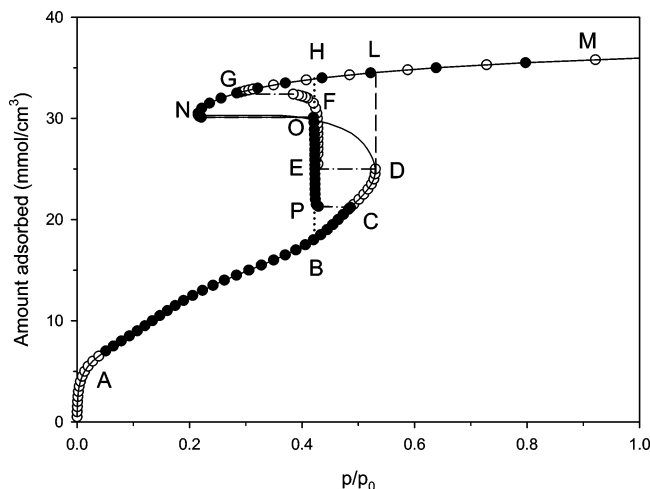


Figure 1. Theoretical argon adsorption isotherm in the infinite cylindrical pore of 4 nm diameter for the developed version of canonical NLDFT. Filled points and open points denote the desorption and adsorption branches, respectively. Explanations are in the text.

$\delta r = \delta z = 0.1\sigma_{ff}$). Since the total amount n is specified, the condition of minimum Helmholtz free energy F requires all partial derivatives of F with respect to $n_{j,k}$ to be equal to the same value μ , which is simply the chemical potential

$$\left(\frac{\partial F}{\partial n_{j,k}}\right)_n = \mu \quad (1)$$

The ideal part of the chemical potential is proportional to the logarithm of density. It allows us to propose the following iteration procedure:

$$n_{j,k}^{(l+1)} = n_{j,k}^{(l)} \exp\left[\frac{\mu - \partial F / \partial n_{j,k}}{\omega k_B T}\right], \quad j = 1, \dots, N, \quad k = 1, \dots, M \quad (2)$$

where l is the number of iteration, k_B is the Boltzmann constant, and ω is an arbitrary number greater than unity, which is introduced to stabilize the iterative procedure. Since the sum of numbers $n_{j,k}$ is specified, the summation of the above equations with respect to k yields

$$\sum_{j,k} \frac{n_{j,k}}{n} \exp\left[\frac{\mu - \partial F / \partial n_{j,k}}{\omega k_B T}\right] = 1 \quad (3)$$

This equation may be rearranged as follows:

$$\mu = -\omega k_B T \ln \xi$$

$$\xi = \sum_{j,k} \frac{n_{j,k}}{n} \exp\left[\frac{-\partial F / \partial n_{j,k}}{\omega k_B T}\right] \quad (4)$$

Initial values for $n_{j,k}$ were taken from the previous equilibrium density distribution at a lower or higher total number of molecules n after multiplying all $n_{j,k}$ by a coefficient to get new value of n . Given the chemical potential μ as solution of the above iteration procedure, the corresponding pressure in the bulk phase could be determined by the NLDFT for the homogeneous fluid. The described iteration scheme is reliable and quite fast.

3. Results

3.1. Argon Adsorption Isotherm in Close Cylindrical Pore.

In Figure 1, we present the adsorption isotherm for an infinite

pore of diameter 4 nm. This isotherm was obtained using the canonical ensemble. At relatively small pressures, the core of the cylindrical pore is empty and the liquidlike film wets the pore walls. The increase of the bulk pressure leads to thickening of the liquidlike film (the part $ABCD$ of the isotherm) up to the vaporlike spinodal point D , where the liquid film loses its mechanical stability and capillary condensation occurs. In this point, the tangent of the isotherm is infinity, which means that a small change in the bulk pressure leads to an extremely large change in the amount adsorbed. In other words, at the vaporlike spinodal point, the density fluctuations become so large that the system spontaneously comes to the more thermodynamically favorable state, which corresponds to the coexistence of the two phases. One of these phases is the liquidlike section of the pore, whereas in the other section the core is empty but its wall is covered with adsorbed molecules. These phases are separated by a meniscus, whose properties are considered below. The section BCD is the metastable adsorption branch of the isotherm since the grand thermodynamic potential is larger than that corresponding to the vapor–liquid coexistence. However, to evolve from the uniform density distribution along the axial direction (liquid film on the wall and empty core) to the two-phase configuration, the system needs to overcome a potential barrier of nucleation to form the initial bridge, which would grow immediately upon the complete filling of the pore. The density functional theory does not consider the density fluctuations, which could lead to the nucleation. Hence, the redistribution of density leading to the state corresponding to smaller Helmholtz free energy could occur only at the spinodal point, where the potential barrier is zero. We always observed such redistribution in finite pores. Interestingly, infinite pore calculations performed with the 2D DFT show that the capillary condensation does not occur spontaneously not only at the vaporlike spinodal pressure but even in the backward (thermodynamic unstable) branch of the isotherm. The solid line is calculated with the two-dimensional version of NLDFT, with the density distribution being axially uniform along the whole adsorption branch of the isotherm. To provide the density redistribution at the vaporlike spinodal point, we artificially disturbed the system by imposing a very small external potential field on one of the boundaries, and then we removed this field allowing the system to come to the lower Helmholtz free energy. As a result, the bulk pressure jumps to the point E , corresponding to the equilibrium transition pressure at which the pore accommodates two distinct phases. One phase occupies part of the pore, which is completely filled with adsorbate, whereas the other phase (vaporlike) consists of adsorbed film and an empty core. These two phases are in equilibrium with each other, separated by a hemispherical meniscus. Further increase of the amount adsorbed occurs at constant pressure, which is the equilibrium transition pressure. This increase of the amount adsorbed is associated with a shift in the meniscus position such that the liquidlike phase is greater at the expense of the vaporlike phase. At point F , the vertical part of adsorption isotherm terminates because the vaporlike phase has been reduced to the small bubble that is no longer stable because of the great interfacial energy. As a result, this small bubble will disappear at the point F . At that instant, the pore is uniformly filled by stretched liquid, resulting in a reduction in pressure from the equilibrium transition pressure to a new pressure, labeled as point G in Figure 1. Further increase of loading leads to the increase of the chemical potential and, consequently, the bulk pressure. During desorption the isotherm goes along the curve $MLHGN$ up to the liquidlike spinodal point N , where the

adsorbed phase represents the mostly stretched liquid, particularly at the pore axis. As a measure of pressure force, we use the following equation to estimate the magnitude of this force. It is taken as the difference between the molecular Gibbs free energy and Helmholtz energy per unit volume

$$\Pi(r,z) = \rho(r,z)[\mu - f(r,z)] \quad (5)$$

where $\rho(r,z)$ and $f(r,z)$ are the local density and the molecular Helmholtz free energy, respectively, r is the distance from the pore axis, and z is the coordinate in axial direction. At the liquidlike spinodal point the above equation gives -314 atm for the homogeneous fluid at the pore axis ($r = 0$). Interestingly, this value exactly coincides with the minimal pressure on the pressure–density diagram for argon at 87.3 K. This diagram was obtained with NLDFT for homogeneous fluid (i.e., in the absence of the external field). Thus, a small decrease in the adsorbed average density leads to the splitting of the adsorbed phase into the liquidlike and the vaporlike sections separated by the hemispherical meniscus. At that instant, the bulk pressure jumps to the equilibrium transition pressure, labeled as point *O* in Figure 1. Further decrease of the average density of the adsorbed argon occurs at constant equilibrium pressure and is accomplished with a shift in the meniscus position to increase the volume occupied by the vaporlike phase. The vertical segment *OP* points to the coexistence of the vaporlike and liquidlike phases. The decrease of amount adsorbed means the evaporation of the liquidlike segment at the equilibrium transition pressure. At the point *P*, the liquidlike section is relatively small. Since we use the mirror-image boundary conditions, the liquidlike section presents a narrow bridge at this point. Any further narrowing makes this bridge unstable and leads to its complete evaporation resulting in an increase in pressure. As a result, the density distribution becomes homogeneous along the pore axis, in the form of liquidlike film on the pore wall, and the core is vaporlike. The pressure increases and the system transfers to the point *C* on the metastable section of the isotherm. Further decrease of the amount adsorbed and the corresponding bulk pressure occur reversibly along the same path as the adsorption branch of the isotherm.

The next series of figures gives a visualization of the adsorption and desorption mechanism. Figure 2 shows argon density distribution at some characteristic points of the adsorption branch of the isotherm. The onset and the end of the adsorbed argon spatial rearrangement corresponding to the *DE* transition are shown in Figure 2, panels a and b. Density distribution is plotted in the form of contour lines in the cylindrical segment of the infinite pore, which consists of the simulation cell and its mirror image. Hence, the length of this pore segment is 40 collision diameters. Initially at the spinodal pressure, the adsorbate presents the liquid film uniformly distributed over the pore walls (Figure 2a). The addition of a small amount adsorbed leads to spontaneous density redistribution with the appearance of two coexisting phases. Since the right part of the pore is the mirror image of the left part, the liquidlike section has a form of a bridge. A significant part of the liquidlike film initially uniformly spread on the pore wall transfers to the core of the section, which is now completely filled by the liquidlike argon. In the canonical ensemble, the total number of molecules is specified; therefore, the thickness of the adsorbed film decreases in the section where the core is empty. The vapor–liquid interface is clearly seen in the figure and has a form close to the hemispherical meniscus. The increase of the amount adsorbed leads to shrinking of the vaporlike section, which eventually transforms to a small bubble. Figure

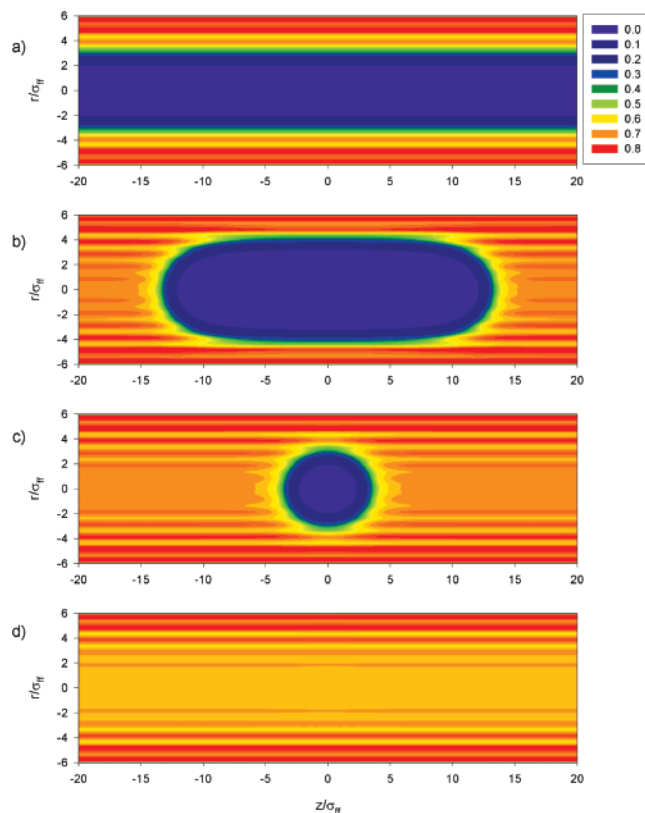


Figure 2. Argon density distribution in the infinite cylindrical pore of 4 nm diameter along the adsorption branch of the isotherm. Different plots correspond to following points of the isotherm depicted in Figure 1: (a) – *D*; (b) – *E*; (c) – *F*; (d) – *G*. Contour lines are defined for the specified reduced density $\rho\sigma_H^3$, where ρ is the number argon density, nm^{-3} . The reduced density of liquid argon is 0.76.

2c depicts the density distribution for the limiting case of mechanical stability of the bubble (point *E* on the isotherm). Any further addition of argon molecules to the pore leads to the disappearance of the bubble, followed by axially homogeneous distribution of the liquidlike adsorbed argon (Figure 2d, point *G* in the isotherm presented in Figure 1). The density distribution of adsorbed argon during desorption is shown in Figure 3 for some characteristic points. At the liquidlike spinodal pressure (point *N* in the isotherm), the density distribution is shown in Figure 3a. At this point, the state of adsorbed argon is close to highly stretched liquid (at a hydrostatic pressure of -314 atm at the pore axis, as it was mentioned above), which breaks with the removal of some molecules from the pore. Such a break of intermolecular bonds leads to the density redistribution, and the two coexisting phases appeared again (Figure 3b). The limiting case of the mechanically stable liquidlike bridge having a width of about 5 collision diameters is shown in Figure 3c. This bridge breaks in its central part with the decrease of the amount adsorbed resulting in its disappearance and establishing a new equilibrium state corresponding to the liquidlike film uniformly covering the pore wall (Figure 3d). Note that the increase of simulation cell length shifts points *F* and *P* toward points *H* and *B*, respectively. Hence, in the limiting case of infinitely long simulation cell the isotherm will not have the segments *FG* and *PC*.

3.2. Free Energy of the Hemispherical Meniscus and the Surface Tension. **3.2.1. Excess Free Energy of the Vapor–Liquid Interface inside the Cylindrical Pore.** Capillary condensation is accompanied by formation of two menisci that bound to the liquidlike section of the pore. This requires an interfacial energy to sustain these menisci. In this respect, we may treat

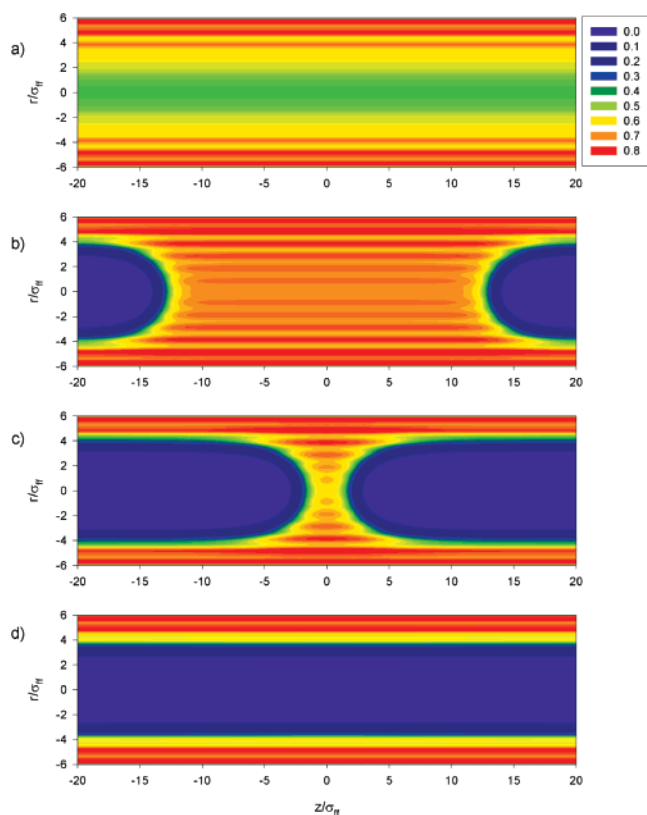


Figure 3. Argon density distribution in the infinite cylindrical pore of 4 nm diameter along the desorption branch of the isotherm. Different plots correspond to following points of the isotherm depicted in Figure 1: (a) – *N*; (b) – *O*; (c) – *P*; (d) – *C*.

the Helmholtz free energy needed for the formation of these two menisci as a measure of nucleation barrier for the capillary condensation at the equilibrium transition pressure. Let us now test this argument. The Helmholtz free energy of one meniscus may be estimated as follows. The meniscus separates the vaporlike and liquidlike sections, which are in thermodynamic equilibrium. Consequently, the grand thermodynamic potential related to unit pore volume for these sections $\bar{\Omega}_V$ and $\bar{\Omega}_L$ (and determined sufficiently far away from the meniscus) is the same. If the meniscus is located approximately in the middle of the simulation cell, so that it does not distort the longitudinally uniform density distribution in the vicinity of the cell boundaries, the excess Helmholtz free energy associated with the meniscus will be given by

$$\Delta F(r) = F(r) - 2\pi \int_0^r r[(L - M_1(r))\rho(r,0)f(r,0) + M_1(r)\rho(r,L)f(r,L)] dr \quad (6)$$

where

$$F(r) = 2\pi \int_0^L \int_0^r r\rho(r,z)f(r,z) dr \quad (6a)$$

$$M_1(r) = \frac{1}{\rho(r,L) - \rho(r,0)} \left[\int_0^L \rho(r,z) dz - L\rho(r,0) \right] \quad (6b)$$

Here $F(r)$ is the Helmholtz free energy of the adsorbed fluid inside the cylindrical volume of radius r , with $F(R)$ being the total Helmholtz free energy of the adsorbed fluid in the simulation cell; R and L are the radius and the length of the cell; M_1 is the first central moment, which defines the equimolar boundary between the coexisting phases in the z direction. In the case of coexisting phases in the pore, the vaporlike phase

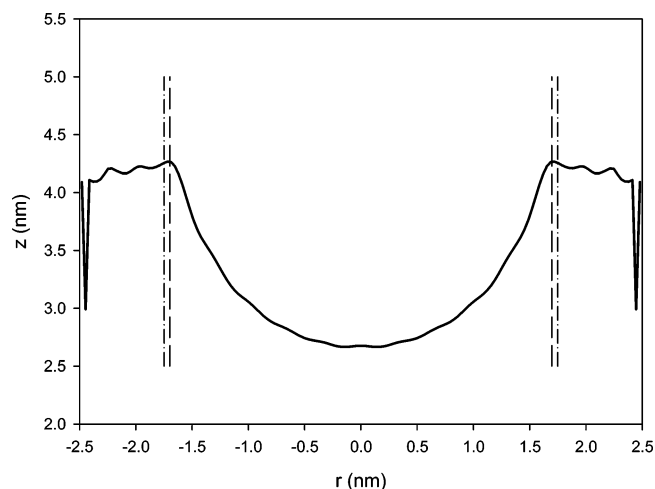


Figure 4. Meniscus shape for the vapor–liquid interface in the cylindrical pore of 5 nm. Ordinate is the first central moment of the density in the longitudinal direction, i.e., the coordinate of the equimolar surface as a function of the distance from the pore axis. The length of the simulation cell is 20 argon collision diameters (6.61 nm). Vertical dashed lines denote the cylindrical surface of tension, along which the resulting pressure acting in axial direction is zero. Vertical dash–dotted lines denote the equimolar cylindrical surface for the vaporlike section of the adsorbed phase. Note that there is the liquid–liquid interface between the surface of tension and the pore wall surface.

is at the left boundary of the cell, whereas the liquidlike phase is at the right boundary. The first central moment M_1 is a function of the distance from the pore axis r , which reflects the shape of the liquid–vapor interface. The dependence of M_1 on the distance r is presented in Figure 4 for the pore diameter of 5 nm. Dashed and dash–dotted vertical lines denote the surface of tension (which will be defined below) and the equimolar surface, respectively, for the section of the simulation cell with the vaporlike core and liquidlike film on the pore wall. An interesting observation is that the meniscus is not strictly hemispherical, with the contact angle being not zero in the proximity of the surface of tension. Another feature is that the fluid is not homogeneous along the z direction even between the pore wall and the cylindrical surface of tension. The density in the completely filled section of the pore is always greater than that in the section with empty core and wetted pore wall. The consequence is that some excess Helmholtz free energy is accumulated in the liquid–liquid interface between the pore wall and the surface of tension.

Figure 5 gives a representation on the differential excess Helmholtz free energy distribution over the cross section of the pore having a diameter of 5 nm. The ordinate is the excess Helmholtz free energy ΔF related to unit of area of the cross section, i.e., the derivative $d\Delta F/d(\pi r^2)$. It is seen from the figure that this change of excess Helmholtz free energy with respect to area is greatest at conjugation line between the meniscus and the surface of tension. The total excess Helmholtz free energy associated with the vapor–liquid interface is given by eq 6. The dependence of the excess free energy related to $k_B T$ on the pore diameter is plotted in Figure 6. There are two downward spikes in the curve, which are possibly associated with a density redistribution accompanying the change of the pore size. The formation of a bridge across the pore involves two menisci, so the excess Helmholtz free energy of the bridge must be multiplied by 2. For example, the energy required for the formation of the bridge as a nucleus of the capillary condensation in the pore of 3.67 nm diameter is about $123k_B T$, which does represent a very significant barrier. Overcoming this great

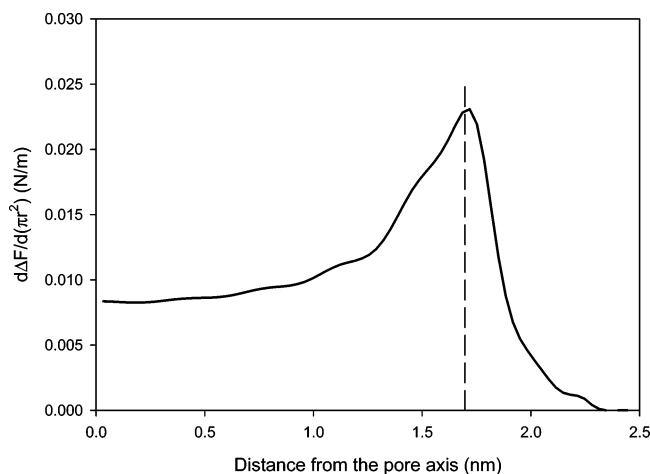


Figure 5. Differential excess Helmholtz free energy of the vapor–liquid (to the left from the dashed line) and liquid–liquid (to the right from the dashed line) interface between the vaporlike and the liquidlike coexisting phases of argon at 87.3 K in the cylindrical pore having diameter of 5 nm. Vertical dashed line denotes the location of the surface of tension.

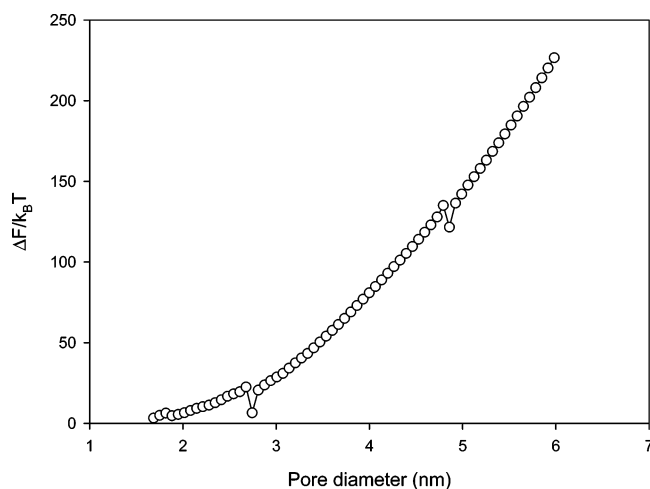


Figure 6. Excess Helmholtz free energy of the vapor–liquid interface between two coexisting phases at the equilibrium transition pressure as a function of the pore diameter for the system Ar–cylindrical silica-like pore at 87.3 K.

barrier by purely density fluctuation is very unlikely. On the other hand, experimentally the hysteresis loop for such pores is not observed suggesting that the potential barrier is indeed overcome. We will discuss this problem below.

3.2.2. Pressure Change across the Vapor–Liquid Interface. The variable as a measure of pressure force, Π , inside the adsorbed phase may be determined by eq 5. The grand thermodynamic potential Ω of n molecules is the integral of $-\Pi$ over the volume, in which these molecules occupy. In the case of longitudinally homogeneous fluid, the average pressure in the cross section is given by

$$\bar{\Pi}(z) = -\frac{2}{R^2} \int_0^R \rho(r,z) [f(r,z) - \mu] r dr = -\bar{\Omega} \quad (7)$$

For coexisting phases, the specific grand potentials $\bar{\Omega}_V$ and $\bar{\Omega}_L$ are equal to each other; that is, the pressure on the left boundary equals that on the right boundary of the simulation cell. It means that the resulting force acting on the cell is zero, which is a condition of its mechanical equilibrium. Figure 7 shows the difference $\Delta\Pi$ between pressures in the liquidlike and vaporlike

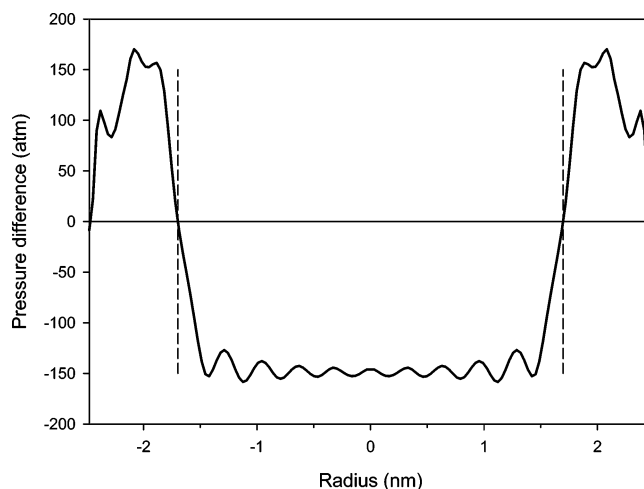


Figure 7. Variation of the pressure difference under and above the meniscus with the distance from the pore axis for the system Ar–silica-like cylindrical pore at 87.3 K. The pore diameter is 5 nm. The negative pressure difference in the central part of the pore means that the liquidlike adsorbed argon is stretched due to two menisci bounded this liquidlike section. The integral of $\Delta\Pi$ over the entire cross section is zero, which is required by the condition of mechanical equilibrium of the adsorbed fluid in the simulation cell. The latter has a consequence that in the proximity of the pore wall the pressure in the filled part of the pore is larger than that in the liquidlike film adjoining the vaporlike core. Vertical dashed lines denote the surface of tension, along which $\Delta\Pi$ is zero.

sections of the pores versus the distance from the pore axis. This pressure difference we determine as follows:

$$\Delta\Pi(r) = \Pi(r,L) - \Pi(r,0) \quad (8)$$

where the pressure Π is defined by eq 5. The pore diameter is 5 nm. This difference is negative in the vicinity of the pore axis, which reflects the fact that the pressure under the concave meniscus is lower than that above the meniscus due to the surface tension. It is important to note that $\Delta\Pi$ is positive in the vicinity of the pore wall, which is a consequence of the mechanical equilibrium of the system. The cylindrical surface of zero value of the pressure difference $\Delta\Pi$ may be identified with Gibbs surface of tension because the tension at this surface balances two equal (in absolute value) forces. The surface of tension does not coincide with the equimolar surface. In the case shown in Figures 4 and 7, the radius of the surface of tension is less by 0.052 nm than that for the equimolar surface. This difference is a monotonically increasing function of the pore radius, which is negative for pore radii less than 1.18 nm and tends to approximately 0.1 nm for large mesopores. In the vicinity of the pore axis, the $\Delta\Pi$ profile resembles a plateau, which is a condition of the hemispherical form of the meniscus. However, $\Delta\Pi$ decreases in its absolute value at positions closer to the surface of tension causing a deviation of the pore shape from hemispherical form. The latter was discussed in the previous section and is seen from Figure 4. Some oscillation of $\Delta\Pi$ is due to the packing effect, i.e., layered structure of the adsorbed fluid.

3.3. Potential Barrier of Nucleation in Cylindrical Pore.

As is known,^{14,33} experimental data show the reversibility of argon and nitrogen isotherms for substantially larger pore sizes than is predicted by the density functional theory. One of the reasons for such disagreement could be the instability of the liquid film adsorbed on the pore walls due to density fluctuations^{56,57} or/and excitation of dynamic waves.^{58–59} Both reasons could lead to overcoming the potential barrier during adsorption

at a pressure lower than the vaporlike spinodal point. We investigate this phenomenon in the grand canonical ensemble.

If the bulk pressure is less than that for the spinodal point, there is a potential barrier, which separates the local and global minima of the grand thermodynamic potential. Hence, despite the fact that the complete filling of the pore is thermodynamically favorable at pressures higher than the equilibrium transition pressure, the potential barrier could hamper the capillary condensation. Such a barrier may be overcome due to the density fluctuations, the surface roughness, or the energetic heterogeneity. In all cases, the spontaneous pore filling starts from the appearance of a nucleus. We proceed from the assumption that the mechanism of the nucleation is not crucial in terms of the value of the potential barrier. It gives the possibility to analyze the potential barrier by imposing an external potential field (so-called ghost field) to force the capillary condensation to occur. This idea was exploited recently in the framework of GCMC simulations.⁵⁷ In this work, we use the external potential field in the form of the Gaussian function

$$u^{\text{ext}} = \frac{\lambda}{\sqrt{2\pi}\Delta} \exp\left[-\left(\frac{z-z_0}{\sqrt{2}\Delta}\right)^2\right] \quad (9)$$

This potential is uniform along the radial direction and changes only in the z axis. The standard deviation Δ should be sufficiently small, since otherwise a large number of molecules would be involved in the density rearrangement under the influence of the field resulting in overestimation of the minimal energy required for the nucleation. Here we used the value of one collision diameter. Imposing of the external potential field leads to the rearrangement of the density distribution in the vicinity of the minimum of the potential. To do this, a work is required. We define this work as the difference between interaction potential of the adsorbed fluid with the external field before the rearrangement has started and after the establishment of equilibrium state

$$\Delta U = \int u^{\text{ext}}(z)[\rho^0(\mathbf{r}) - \rho(\mathbf{r})] d\mathbf{r} \quad (10)$$

Here $\rho^0(\mathbf{r})$ and $\rho(\mathbf{r})$ are the density corresponding to the equilibrium distribution without the external field and that after the field was imposed. The above equation accounts for the work required only for the displacement of molecules in the external field reflected by the term in square parenthesis of the integrand. This displacement takes some time; therefore, at the instant of imposing of the external field, molecules have the same positions as those when the external potential was zero. Hence, before the molecules have changed their positions, no work is consumed, much as the external potential is. The magnitude of this work depends on the multiplier λ in eq 9. Gradually tuning the multiplier, we can achieve the situation when the system loses its mechanical stability and spontaneous condensation will occur. This critical point corresponds to the potential energy required for the molecular rearrangement, which may be identified as the potential barrier for nucleation.

Figure 8 shows the density distribution in the cylindrical pore having a diameter of 4 nm under the influence of the external field. The reduced bulk phase pressure is 0.45, which is slightly larger than the equilibrium transition pressure (0.422) and lower than the vaporlike spinodal pressure (0.53). The parameter λ in this case is $17.8k_B T$. The density distribution at this value of the parameter corresponds to the limiting case of mechanical stability of the liquid film on the pore wall. It is seen from the figure that the critical nucleus has the form of bump rather than

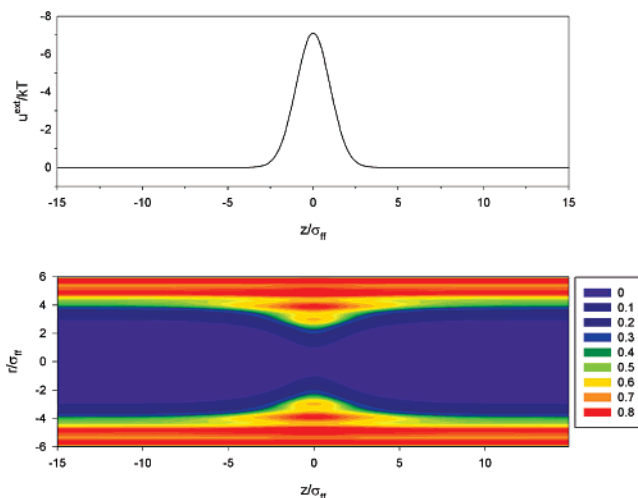


Figure 8. Nucleation induced by the external field. The density distribution at $p/p_0 = 0.45$ and $D = 4$ nm for the limiting case of mechanical stability of the liquidlike film (the lower plot). The upper plot shows the distribution of external potential imposed to the adsorbed fluid.

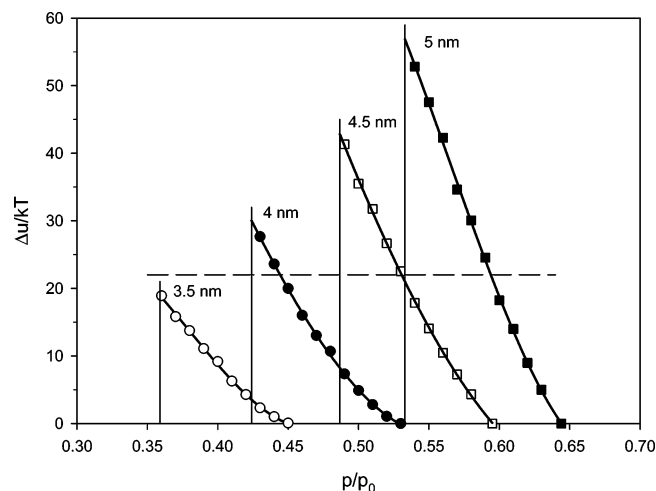


Figure 9. Dependence of the potential barrier on the bulk pressure for the system Ar–cylindrical pore of MCM-41 samples at 87.3 K. The pore diameter (nm): (○) 3.54, (●) 4.0, (□) 4.53, (■) 5.0. Vertical lines correspond to equilibrium transition pressures.

bridge, which is in agreement with the Everett and Haynes scenario.⁶⁰ The same result obtained from GCMC simulations was reported by Vishnyakov and Neimark.⁵⁷ The density in the pore center is about 100 times less than the density of liquid argon.

Dependences of the potential barrier on the bulk pressure for different pore diameters are shown in Figure 9. As is seen from the figure, the increase of pressure toward the vaporlike spinodal point decreases the potential barrier. At the spinodal point, the potential barrier becomes zero and the maximal value of the potential barrier is at the equilibrium transition pressure, which is denoted by a vertical line for the corresponding pore diameter. Experimental data on argon adsorption in cylindrical pores of MCM-41 silica samples indicate that the isotherm at 87.3 K is reversible for pore sizes less than approximately 3.8 nm. It suggests that the potential barrier corresponding to this pore size at the equilibrium transition pressure is the smallest barrier, which could be overcome due to the density fluctuations. The set of curves plotted in Figure 9 shows that the barrier must exceed $20k_B T$. Let this critical barrier be of $22k_B T$ (dashed line in the figure). In this case, the point of intersection of the dashed line and a descending curve corresponds to the condensation

pressure. Hence, the narrowing of the hysteresis loop, which is observed experimentally, may be at least qualitatively explained by the overcoming of the potential barrier. It is interesting to compare the maximal values of the barrier with the energy needed for the formation of two menisci bounded to the smallest bridge that could be the nucleus of spontaneous condensation. The latter is much higher than the actual minimal energy required for the phase transition, which one can see from Figures 6 and 9. For example, the potential barrier of condensation at the equilibrium transition pressure in the pore of 4 nm is $30k_B T$, whereas the energy accumulated in two menisci of the bridge is $162k_B T$. It is worth noting that the bridge becomes unstable and disappears if its width is less than a few collision diameters, which means that the bump depicted in Figure 8 is also unstable without an external force. One would think that since the spontaneous condensation without imposing of an external force could be nucleated by the bridge rather than the bump, it requires enormous energy making the probability of the condensation extremely low. Nevertheless, the potential barrier significantly decreases due to the imposition of the external field allowing the nucleation to occur in the form of a bump. In real physical situations, such an external field may represent any forces associating with factors such as surface energetic heterogeneity and surface roughness or with excitation of waves having dynamical rather than equilibrium origin. Further investigations of nucleation phenomena are needed to clarify the reversibility.

4. Conclusions

The phase transition of argon at 87.3 K in cylindrical pores having an amorphous pore wall structure like that of MCM-41 silica was considered by means of the canonical ensemble two-dimensional density functional theory. We determined the form of the meniscus separating the liquidlike and the vaporlike coexisting phases, which deviates from the hemispherical meniscus. We considered the mechanism of nucleation by imposing the external potential field in the form of a narrow Gaussian peak. The potential barrier dependence on the pore diameter and the bulk pressure in the region between the equilibrium transition pressure and the spinodal condensation pressure has been evaluated. It was found that the potential barrier of about $22k_B T$ must be overcome due to the density fluctuations in order to provide the experimentally observed adsorption reversibility in the case of argon adsorption for pore sizes up to 3.8 nm. The nuclei have the form of a bump rather than a liquidlike bridge. Further efforts are needed for a deeper analysis of interfacial region properties and the nucleation and the hysteresis phenomena.

Acknowledgment. Support from the Australian Research Council is gratefully acknowledged.

References and Notes

- (1) Everett, D. H. In *The Solid-Gas Interface*; Flood, E. A., Ed.; Marcel Dekker: New York, 1967; Vol. 2, Chapter 36, p 1055.
- (2) Greg, S. J.; Sing, K. S. W. *Adsorption, Surface Area and Porosity*; Academic Press: London, 1982.
- (3) Cohan, L. H. *J. Am. Chem. Soc.* **1938**, *60*, 433.
- (4) Barrett, E. P.; Joyner, L. G.; Halenda, P. P. *J. Am. Chem. Soc.* **1951**, *73*, 373.
- (5) Broekhoff, J. C. P.; de Boer, J. H. *J. Catal.* **1967**, *9*, 8, 15.
- (6) Broekhoff, J. C. P.; de Boer, J. H. *J. Catal.* **1968**, *10*, 368, 377, 391.
- (7) Lukens, W. W., Jr.; Schmidt-Winkel, P.; Zhao, D.; Feng, J.; Stucky, J. D. *Langmuir* **1999**, *15*, 5403.
- (8) Zhu, H. Y.; Lu, G. Q.; Zhao, X. S. *J. Phys. Chem. B* **1998**, *102*, 7371.
- (9) Qiao, S. Z.; Bhatia, S. K.; Zhao, X. S. *Microporous Mesoporous Mater.* **2003**, *65*, 287.
- (10) Qiao, S. Z.; Bhatia, S. K.; Nicholson, D. *Langmuir* **2004**, *20*, 389.
- (11) Sonwane, C. G.; Bhatia, S. K. *Chem. Eng. Sci.* **1998**, *53*, 3143.
- (12) Bhatia, S. K.; Sonwane, C. G. *Langmuir* **1998**, *14*, 1521.
- (13) Sonwane, C. G.; Bhatia, S. K. *Langmuir* **1999**, *15*, 5347.
- (14) Sonwane, C. G.; Bhatia, S. K.; Calos, N. *Ind. Eng. Chem. Res.* **1998**, *37*, 2271.
- (15) Sonwane, C. G.; Bhatia, S. K. *J. Phys. Chem. B* **2000**, *104*, 9099.
- (16) Maddox, M. W.; Olivier, J. P.; Gubbins, K. E. *Langmuir* **1997**, *13*, 1737.
- (17) Gelb, L. D. *Mol. Phys.* **2002**, *100*, 2049.
- (18) Vishnyakov, A.; Neimark, A. V. *J. Chem. Phys.* **2003**, *119*, 9755.
- (19) Coasne, B.; Pellenq, R. J.-M. *J. Chem. Phys.* **2004**, *120*, 2913.
- (20) Ravikovitch, P.; Domhnaill, S.; Neimark, A.; Schuth, F.; Unger, K. *Langmuir* **1995**, *11*, 4765.
- (21) Ravikovitch, P. I.; Wei, D.; Chueh, W. T.; Haller, G. L.; Neimark, A. V. *J. Phys. Chem. B* **1997**, *101*, 3671.
- (22) Neimark, A. V.; Ravikovitch, P. I.; Grün, M.; Schüth, F.; Unger, K. K. *J. Colloid Interface Sci.* **1998**, *207*, 159.
- (23) Ravikovitch, P. I.; Haller, G. L.; Neimark, A. V. *Adv. Colloid Interface Sci.* **1998**, *76–77*, 203.
- (24) Neimark, A. V.; Ravikovitch, P. I.; Vishnyakov, A. *Phys. Rev. E* **2000**, *62*, 1493.
- (25) Ravikovitch, P. I.; Neimark, A. V. *Stud. Surf. Sci., Catal.* **2000**, *129*, 597.
- (26) Neimark, A. V.; Ravikovitch, P. I. *Microporous Mesoporous Mater.* **2001**, *44–45*, 697.
- (27) Ravikovitch, P. I.; Vishnyakov, A.; Neimark, A. V. *Phys. Rev. E* **2001**, *64*, 011602.
- (28) Ravikovitch, P. I.; Neimark, A. V. *Colloids Surf. A: Physicochem. Eng. Aspects* **2001**, *187–188*, 11.
- (29) Neimark, A. V.; Ravikovitch, P. I.; Vishnyakov, A. *J. Phys.: Condens. Matter* **2003**, *15*, 347.
- (30) Cao, D.; Shen, Z.; Chen, J.; Zhang, X. *Microporous Mesoporous Mater.* **2004**, *67*, 159.
- (31) Kresge, C. T.; Leonowicz, M. E.; Roth, W. J.; Vartuli, J. C.; Beck, J. S. *Nature* **1992**, *359*, 710.
- (32) Beck, J. S.; Vartuli, J. C.; Roth, W. J.; Leonowicz, M. E.; Kresge, C. T.; Schmitt, K. D.; Chu, C. T.-W.; Olson, D. H.; Sheppard, E. W.; McCullen, S. B.; Higgins, J. B.; Schlenker, J. L. *J. Am. Chem. Soc.*, **1992**, *114*, 10834.
- (33) Kruk, M.; Jaroniec, M.; Sayari, A. *J. Phys. Chem. B* **1997**, *101*, 3671.
- (34) Franke, O.; Schulz-Ekloff, G.; Rathousky, J.; Starek, J.; Zukal, A. *J. Chem. Soc., Chem. Commun.* **1993**, 724.
- (35) Branton, P. J.; Hall, P. G.; Sing, K. S. W. *J. Chem. Soc., Chem. Commun.* **1993**, 1257.
- (36) Morishige, K.; Ito, M. *J. Chem. Phys.* **2002**, *117*, 8036.
- (37) Morishige, K.; Nakamura, Y. *Langmuir* **2004**, *20*, 4503.
- (38) Kruk, M.; Jaroniec, M.; Sayari, A. *Langmuir* **1997**, *13*, 6267.
- (39) Branton, P. J.; Hall, P. G.; Sing, K. S. W. *J. Chem. Soc., Chem. Commun.* **1993**, 1257.
- (40) Kruk, M.; Jaroniec, M. *J. Phys. Chem. B* **2002**, *106*, 4732.
- (41) Inoue, S.; Hanzawa, Y.; Kaneko, K. *Langmuir* **1998**, *14*, 3079.
- (42) Kruk, M.; Jaroniec, M.; Sayari, A. *Adsorption* **2000**, *6*, 47.
- (43) Vishnyakov, A.; Neimark, A. V. *J. Phys. Chem. B* **2001**, *105*, 7009.
- (44) Ravikovitch, P. I.; Neimark, A. V. *Langmuir* **2002**, *18*, 9830.
- (45) Ustinov, E. A.; Do, D. D. *J. Chem. Phys.* **2004**, *120*, 9769.
- (46) Ustinov, E. A.; Do, D. D.; Jaroniec, M. Application of density functional theory to equilibrium adsorption of argon and nitrogen on amorphous silica surface. *Appl. Surf. Sci.* **2005**, accepted.
- (47) Ustinov, E. A.; Do, D. D.; Jaroniec, M. Adsorption of argon and nitrogen in cylindrical pores of MCM-41 materials: Application of density functional theory. *Appl. Surf. Sci.* **2005**, accepted.
- (48) Ustinov, E. A.; Do, D. D.; Jaroniec, M. *J. Phys. Chem. B* **2005**, *109*, 1947.
- (49) Ustinov, E. A.; Do, D. D. Capillary phenomena in the framework of the two-dimensional density functional theory. *Fundamentals of Adsorption 8*. Sedona, Arizona; May 23–28, 2004.
- (50) Tarazona, P. *Phys. Rev. A* **1985**, *31*, 2672.
- (51) Evans, R.; Marconi, U. M. B.; Tarazona, P. *J. Chem. Soc., Faraday Trans. 2* **1986**, *82*, 1763.
- (52) Tarazona, P.; Marconi, U. M. B.; Evans, R. *Mol. Phys.* **1987**, *60*, 573.
- (53) Carnahan, N. F.; Starling, K. E. *J. Chem. Phys.* **1969**, *51*, 635.
- (54) Weeks, J. D.; Chandler, D.; Andersen, H. C. *J. Chem. Phys.* **1971**, *54*, 5237.
- (55) Kruk, M.; Jaroniec, M. *Chem. Mater.* **2000**, *12*, 222.
- (56) Vishnyakov, A.; Neimark, A. V. *J. Phys. Chem. B* **2001**, *105*, 7009.
- (57) Vishnyakov, A.; Neimark, A. V. *J. Chem. Phys.* **2003**, *119*, 9755.
- (58) Cole, M. W.; Saam, W. F. *Phys. Rev. Lett.* **1974**, *32*, 985.
- (59) Talanquer, V.; Oxtoby, D. W. *J. Chem. Phys.* **2001**, *114*, 2793.
- (60) Everett, D. H.; Haynes, J. M. *J. Colloid Interface Sci.* **1972**, *38*, 125.